

Contents list available at CBIORE journal website

# **International Journal of Renewable Energy Development**

Journal homepage: https://ijred.cbiore.id



Research Article

# Valorization of coal fly ash for the synthesis of lithium nickel-cobaltaluminum-iron oxide (NCAF) cathode material

Conelius Satria Yudha <sup>a,b,\*</sup> , Aleida Dwi Rahmawati<sup>a</sup>, Ragil Sumarti<sup>a</sup>, Soraya Ulfa Muzayanha<sup>c</sup>, Annisa Puji Lestari<sup>b,d</sup>, Meidiana Arinawati<sup>b</sup>

**Abstract**. This study demonstrates a novel approach to high-performance cathode materials by utilizing coal fly ash as a source of Al and Fe dopants for nickel-rich layered oxides. LiNi<sub>x</sub>Co<sub>y</sub>Al<sub>z</sub>Fe<sub>(1-xy-z)</sub>O<sub>2</sub> (NCAF) materials were synthesized through a combined hydrometallurgical-solid state route, incorporating fly-ash waste-derived Al/Fe hydroxides (AFH) at various concentrations during the lithiation process. The characteristics of NCAF precursors, AFH and Ni<sub>0.8</sub>Co<sub>0.2</sub>C<sub>2</sub>O<sub>4</sub>, were thoroughly investigated. Structural analysis confirms the successful formation of single-phase materials with α-NaFeO2 structure (R-3m) up to 5% AFH content, exhibiting changes in the level of order, lattice parameters, and unit cell volume. Surface area characteristics show a transition from 38.747 m²/g to 6.52 m²/g with increasing AFH content, approaching the ideal surface area. The compositional evolution from LiNi<sub>0.8</sub>Co<sub>0.2</sub>O<sub>2</sub> to LiNi<sub>0.66</sub>Co<sub>0.16</sub>Al<sub>0.08</sub>Fe<sub>0.10</sub>O<sub>2</sub> maintains uniform atomic distribution. In the full-cell configuration with graphite anodes (N/P ratio: 1.2-1.3), NCAF with 5% AFH demonstrates enhanced electrochemical performance (~155 mAh/g), attributed to synergistic effects of Alinduced structural stabilization and Fe-contributed redox activity. This approach establishes a pathway for simple and low-cost battery material development while addressing industrial waste utilization.

Keywords: Fly ash, Cathode, Characterization, Li-ion battery, Nickel, Waste



@ The author(s). Published by CBIORE. This is an open access article under the CC BY-SA licenses (http://creativecommons.org/licenses/by-sa/4.0/).

Received: 10th Nov 2024; Revised: 6th January 2025; Accepted: 26th January 2025; Available online: 4th Feb 2025

#### 1. Introduction

The global demand for energy storage continues to increase, driven by the growing energy needs of electronic devices, industry, and long-term transportation (Chandrasekharam *et al.*, 2024). Simultaneously, the Paris Climate Agreement of 2015 introduced the Net Zero Emissions (NZE) program, aiming to reduce environmental pollution and mitigate global warming. Energy production and storage are crucial factors in achieving NZE goals. As fossil fuel reserves are depleting along with the increasing generated waste or emissions, there is an urgent need for renewable energy storage solutions (Lagouir *et al.*, 2021).

Lithium-ion batteries have emerged as a promising technology for cleaner energy production. These rechargeable electrochemical cells, composed of a negative electrode (anode) (Mopoung *et al.*, 2021), positive electrode (cathode) (Sudaryanto *et al.*, 2024), electrolyte, and separator(Rahmawati *et al.*, 2024), can store electrical energy for extended periods. Currently, many research focuses on improving battery performance through electrode enhancement. One notable advancement in lithium-ion battery technology is the development of Ni-rich

cathode-containing batteries, especially the layered Lithium Nickel Cobalt Aluminum Oxide (LiNi $_x$ Co $_y$ Al $_z$ O $_2$  or NCA) batteries. However, there is still room for improvement in terms of capacity and sustainability(Purwanto *et al.*, 2018).

Fly ash, a by-product of coal combustion, presents significant environmental challenges due to its high content of heavy metals and difficulty in processing (Mathapati *et al.*, 2021). However, its composition, particularly the presence of Al<sub>2</sub>O<sub>3</sub> and Fe<sub>2</sub>O<sub>3</sub>, makes it a potential raw material for battery production (Y. Zhang *et al.*, 2019). Despite this potential, few studies have specifically investigated the extraction of SiO<sub>2</sub> (Jumari *et al.*, 2020), Al<sub>2</sub>O<sub>3</sub>, and Fe<sub>2</sub>O<sub>3</sub> from coal fly ash (Zhang *et al.*, 2019). This has led to potential modifications, such as the incorporation of coal fly ash waste, resulting in fly ash-derived active anode and cathode materials. The silicon-based anode has been extensively studied. However, extraction of Si from fly ashes often produces secondary Al and Fe-containing residue (Liu *et al.*, 2022).

Recent research has focused on overcoming challenges in NCA synthesis and improving its performance. Advanced co-

<sup>&</sup>lt;sup>a</sup>Chemical Engineering Department, Vocational School, Sebelas Maret University, Surakarta, Central Java, Indonesia

<sup>&</sup>lt;sup>b</sup>Centre of Excellence for Electrical Energy Storage Technology, Sebelas Maret University, Surakarta, Central Java, Indonesia

<sup>&</sup>lt;sup>c</sup>Pertamina Technology Innovation, PT. Pertamina, Pulogadung, Jakarta, Indonesia

<sup>&</sup>lt;sup>d</sup>Graduate School of Engineering, Hokkaido University, Hokkaido, Japan

<sup>\*</sup>Corresponding author Email: corneliussyudha@staff.uns.ac.id (C.S.Yudha)

precipitation methods using various chelating agents like ammonia, 5-sulfosalicylic acid (Xie et al., 2015), oxalic acid (Nisa et al., 2021) and EDTA (Xie et al., 2016) have shown promise in enhancing material. Doping strategies, particularly with elements like Fe, have emerged as effective ways to improve electrochemical properties. Kim *et al.* reported that Fe doping in LiNi<sub>0.85</sub>Co<sub>0.10</sub>Al<sub>0.05</sub>O<sub>2</sub> enhanced performance at elevated temperatures, improving capacity retention and cycle life (Kim et al., 2014). Other dopants such as Mg (Lv et al., 2020), Ti, and Mn (Wan et al., 2018) have also been explored, each offering unique benefits in structural stability and ion diffusion. Surface modification techniques, including coatings with metal oxides, fluorides, and phosphates, have been developed to protect NCA particles from side reactions with the electrolyte, especially at high temperatures and voltages (Seenivasan et al., 2022). These coatings significantly improve the cycling stability and thermal properties of NCA cathodes. Despite these advancements, challenges remain in achieving consistent quality at scale while minimizing production costs and environmental impact (Purwanto et al., 2018). In fact, the co-precipitation of NCA precursor is often challenged by the difficulties of Al incorporation during the precipitation owing to differences in  $K_{sp}$  value (K. He *et al.*, 2017). Extensive researches continue to explore optimal combinations of synthesis techniques, dopants, and coatings to meet the growing demand for highperformance, stable NCA cathode materials in the expanding lithium-ion battery market (Wang et al., 2023). The doping technique is promising to be adapted due to its simplicity. This opens the opportunity to improve the characteristic of NCA by Fe and Al doping from coal fly ash. Herein, this research addresses this technological gap by utilizing fly ash as a component in Fe-doped NCA (NCAF) cathode materials. Al and Fe were extracted and isolated through hydrometallurgical processes such as leaching and chemical precipitation. The precipitate was then used as a material for the synthesis of NCAF. The optimum composition was investigated by varying the dopant content during the synthesis. This approach serves multiple purposes by mitigating environmental problems caused by fly ash waste, Enhancing the efficiency and durability of NCAF batteries, and increasing the economic value of waste processing. By repurposing fly ash for battery production, this study presents an innovative solution to waste management while contributing to the development of more sustainable lithium-ion batteries.

# 2. Materials and Methods

# 2.1 Materials

Waste fly ash was obtained from PT Paiton Energy (Indonesia) in fine powder form. The fly ash was obtained using an electrostatic precipitator installed in the flue gas pathway. Analytical grade sulfuric acid ( $H_2SO_4$ , 95-97%, Merck, Germany) was used as a leaching agent to extract  $Al_2O_3$  and  $Fe_2O_3$  and avoid the extraction of Ca. Sodium hydroxide (NaOH,  $\geq$ 98%, Asahi, Indonesia) was used as a precipitating agent. All other chemicals used were of analytical grade and used without further purification.

#### 2.2 Methods

# 2.2.1 Recovery of Iron and Aluminum from Fly Ash Waste

The recovery process was initiated by mixing 100 g of fly ash with 200 g of  $Na_2CO_3$ . The mixture was heated inside a crucible at 900°C for 5 hours to obtain a clinker. The clinker was then ground and added to DI water at 80-90°C for 2 hours to

**Table 1**The mass composition of NCO and AFH for the preparation of NCAF precursor

NCAF variations	NCO %mass	AFH %mass
NCAF0	100	0
NCAF2.5	97.5	2.5
NCAF2.5	95.0	5.0
NCAF7.5	92.5	7.5

form a slurry. The slurry was filtered, and the residue was dried. At this point, a large amount of  $SiO_2$  is reduced(X. Liu *et al.*, 2022).

The dry residue was leached with 1 L of 2 M  $\rm H_2SO_4$  at 80-90°C for 2 hours. The leachate was filtered and rinsed with 500 mL of DI water. The filtrate was heated to 60°C and precipitated using 4 M NaOH until pH 10-11 was reached. The precipitate was filtered, washed with water until neutral pH, and ovendried. This precipitate, consisting of a mixture of Fe(OH) $_3$  and Al(OH) $_3$ , was designated as the AFH precursor.

#### 2.2.2 Preparation of Ni<sub>0.8</sub>Co<sub>0.2</sub>C<sub>2</sub>O<sub>4</sub> (NCO precursor)

The NC precursor was synthesized by dissolving 0.8 mol of NiSO $_4$ -6H $_2$ O and 0.2 mol of CoSO $_4$ -7H $_2$ O in 1 L of distilled water at 60°C. To this solution, 1 mol of C $_2$ H $_2$ O $_4$  and 2 mol of NaOH were added to achieve a pH of 2-3, resulting in precipitation of a pale green powder. The mixture was maintained at 60°C with continuous stirring for 2 hours. The precipitate was filtered, washed with DI water until neutral pH, dried, ground, and sieved through a 200-mesh screen.

#### 2.2.3 Synthesis of NCAF Precursor

The NCAF precursor was prepared by mixing the NCO precursor ( $Ni_{0.8}Co_{0.2}C_2O_4$ ) with the AFH precursor (Al(OH)<sub>3</sub> and Fe(OH)<sub>3</sub>) in various mass ratios, as shown in Table 1. The mixtures were homogenized using a mortar and pestle.

#### 2.2.4 Calcination and sintering process

The NCAF precursor (200 g) was mixed with LiOH·H $_2$ O (50 g) using a mortar and pestle. The mixture was transferred to a porcelain crucible and calcined at 500°C for 5 hours under  $O_2$  flow in a muffle furnace. After that, the samples were sintered at 750°C for 12 hours under  $O_2$  flow to improve the crystalline property and density of the material.

# 2.2.6 Characterization of materials

Fourier-Transform Infrared Spectroscopy (FTIR, IR-Spirit, Shimadzu, Japan) analysis was employed to investigate the presence of functional groups in the materials. X-ray diffractometer (XRD, Bruker Phaser, Germany) was used to analyze the crystal phase and structure of the material. The morphology and the element compositions were examined using Scanning Electron Microscope-Energy Dispersive X-ray Spectroscopy (SEM-EDX, JCM 7000, JEOL, Japan). The precursors' thermal properties were examined using Thermogravimetry- Differential Temperature Analysis (TG/DTA, TGA-60, Shimadzu). Surface area analysis of the NCAF samples was determined using  $N_2$  adsorption-desorption isotherm (Quantachrome Nova, Quantachrome Instruments, USA).

#### 2.2.7 NCAF Electrode Fabrication

NCAF electrodes were prepared by mixing the active material with conductive additives and binders. The

composition was as follows: 90 wt% NCAF, 3 wt% acetylene black (AB), 2 wt% carboxymethyl cellulose (CMC), 3 wt% styrene-butadiene rubber (SBR), and 2 wt% oxalic acid. The components were mixed using a mortar and pestle to form a slurry, which was then coated onto aluminum foil (200  $\mu m$  thick) using a doctor blade technique. The coated electrodes were dried at room temperature for 24 hours, followed by vacuum drying at 120°C for 12 hours. Commercial Graphite electrode was used as the counter anode and provided by PT Batex Energi Mandiri, Indonesia.

#### 2.2.8 Battery Assembly

The negative-to-positive capacity ratio (N/P) was designed in the range of 1.2-1.3 based on the theoretical capacity of graphite (372 mAh/g) and the estimated practical capacity of NCAF materials (200 mAh/g). The electrode loading was adjusted accordingly to achieve the target N/P ratio, ensuring optimal cell performance while maintaining an adequate lithium reservoir in the graphite electrode and avoiding Li-plating(Mu et al., 2022).

The dried NCAF cathode sheets were calendared to a specific density using a roll press. Electrodes were cut into 5.6 cm wide strips using a slitting machine. Aluminum tabs were ultrasonically welded to the cathode sheets. The cathode, separator, and anode were assembled into a jellyroll structure using a winding machine. The jellyroll was inserted into a cylindrical casing with a nickel plate at the bottom serving as the negative terminal. The casing was sealed using a pneumatic welding technique. Electrolyte (1 M LiPF6 in EC: DMC, 1:1 v/v) was injected into the cell in an argon-filled glove box ( $O_2$  and  $H_2O < 0.1$  ppm). The cells were finally sealed with a cap containing a safety vent. The formation cell analysis was performed using Arbin BT1802, USA by employing a current of 10 mA/g at the voltage range of 2.5-4.25 V.

# 3. Results and Discussion

# 3.1 AFH Synthesis from Fly Ash Waste

AFH precursors are synthesized by recovering aluminum and iron from fly ash through roasting (caustic fusion) and acid-leaching processes. The fly ash undergoes leaching with 20% sulfuric acid ( $H_2SO_4$ ) and is then treated with sodium hydroxide (NaOH). The sulfuric acid leaching process effectively isolates  $Al_2O_3$  and  $Fe_2O_3$  from the fly ash waste. Based on EDX data, Fly ash waste contains 25.82% aluminum and 5.30% iron by weight. The chemical reactions during the leaching process for isolating Al and Fe using  $H_2SO_4$  are shown in equation (1), followed by the precipitation reaction with NaOH in equation (2) (Yudha, Apriliyani, *et al.*, 2022).

$$Al_2O_{3(s)} + 3H_2SO_{4(aq)} \rightarrow Al_2(SO_4)_{3(aq)} + 3H_2O_{(l)}$$
 (1)

$$Al_2(SO_4)_{3(aq)} + 6NaOH_{(aq)} \rightarrow 2Al(OH)_{3(s)} + 3Na_2SO_{4(aq)}$$
 (2)

Meanwhile, the chemical reaction in isolating Fe is in equations (3) and (4).

$$Fe_2O_{3(s)}+3H_2SO_{4(aq)} \rightarrow Fe_2(SO_4)_{3(aq)}+3H_2O_{(l)}$$
 (3)

$$Fe_2(SO_4)_{3(aq)} + 6NaOH_{(aq)} \rightarrow 2Fe(OH)_{3(s)} + 3Na_2SO_{4(aq)}$$
 (4)

#### 3.1.1 AFH XRD and FTIR analysis

Figure 1a presents the FTIR analysis of fly ash waste AFH deposits, conducted across the wavenumber range of 4000-400 cm<sup>-1</sup>, identifying chemical bonds and functional groups in the compounds. The spectrum shows several characteristic absorption peaks: a band at 3415 cm<sup>-1</sup> corresponds to hydroxyl

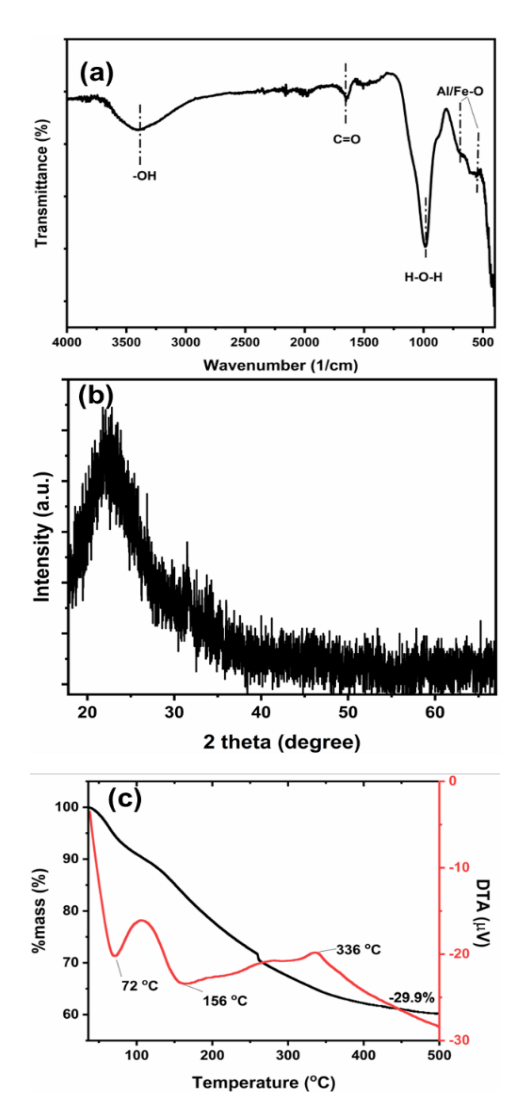
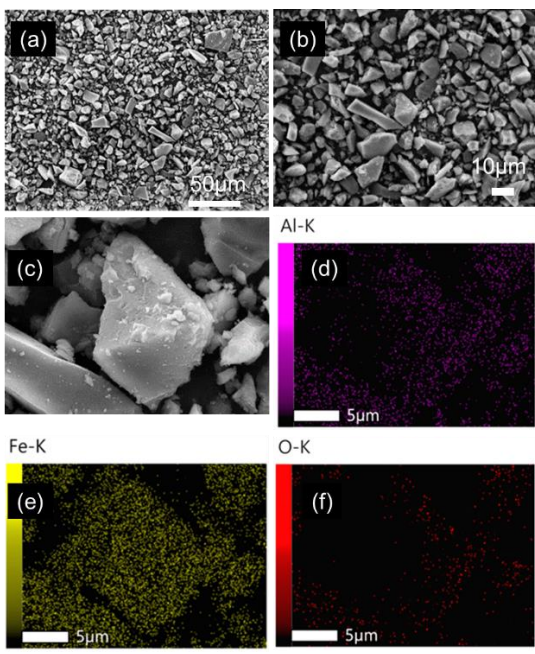


Fig. 1 (a) FTIR Spectra, (b) XRD pattern, and (c) TG/DTA curve of AFH

group (-OH) vibrations from trapped water molecules in the precipitate(Muzayanha et al., 2019). An absorption peak at 2340 cm<sup>-1</sup> is attributed to C-H stretching, while the peak at 1654 cm<sup>-1</sup> represents C=O vibrational bonds. The absorption band at 986 cm<sup>-1</sup> is assigned to Al-O stretching vibrations, and the peak below 697 cm<sup>-1</sup> corresponds to Fe-O stretching modes. The presence of C=O bonds associated with carbonate groups confirms the reactions described in equations 2 and 4 (X. He et al., 2017). The XRD pattern shown in Figure 1b reveals characteristic features of a poorly crystalline or semiamorphous material, consistent with mixed Al/Fe hydroxide phases. The diffractogram is dominated by a broad, intense peak centered in the region of 20-25° 20, which is typical of poorly crystalline Al(OH)3 and Fe(OH)3 structures. This peak broadness suggests small crystallite size and limited long-range structural order, which is common in materials precipitated from aqueous solutions. In the higher angle region (30-60 $^{\circ}$  2 $\theta$ ), the pattern exhibits a gradual decrease in intensity with diffuse, low-intensity peaks, further indicating the predominant amorphous property of the sample (X. He et al., 2017). The noisy character of the pattern and absence of sharp, well-defined peaks is consistent with a material composed of co-precipitated metal hydroxides, likely resulting from rapid precipitation processes. This XRD analysis aligns well with the FTIR data shown in Figure 1(a), where the presence of hydroxyl groups



**Fig. 2** Morphological and elemental analysis of AFH extracted from fly ash: (a,b) SEM images at different magnifications (c) high-magnification SEM image and EDX analysis area, and (d-f) corresponding EDX elemental mapping showing distribution of Al, Fe, and O elements.

 Table 2

 Atomic Composition of AFH Precipitates from Waste Fly Ash

Element	Mass %	Atom %
0	40.06±0.88	66.69±1.46
Al	12.77±0.22	15.74±0.22
Fe	26.89±1.63	10.35±0.79

and metal-oxygen bonds supports the formation of mixed aluminum and iron hydroxide phases.

### 3.1.2 Morphological Characteristic Test Analysis (SEM)

SEM analysis (Scanning Electron Microscopy) is used to analyze the surface morphology structure and particle size or diameter of AFH precipitate. The morphological and elemental analysis of the extracted AFH from fly ash can be observed in Figure 2. Meanwhile, Table 2 displays the compositional characteristics of AFH using EDX. Figure 2(a,b,c) shows particles with irregular morphology but homogenous shapes with wide particle size distribution. The elemental mapping results (d-f) show the particles' successful homogenous O, Fe, and Al distribution. The Al-K (magenta) and Fe-K (yellow) maps demonstrate homogeneous elements, suggesting the formation of mixed metal hydroxide phases rather than segregated singlemetal compounds. The O-K (red) mapping correlates well with the metal distribution, confirming the hydroxide nature of the material. This uniform distribution of Al and Fe is particularly beneficial for their subsequent incorporation as dopants in the cathode material synthesis.

# 3.2 Analysis of NC precursor (Ni<sub>0.8</sub>Co<sub>0.2</sub>C<sub>2</sub>O<sub>4</sub>)

The structural characteristics of the synthesized NC precursor were investigated through complementary analytical techniques presented in Figure 3. The FTIR spectrum reveals

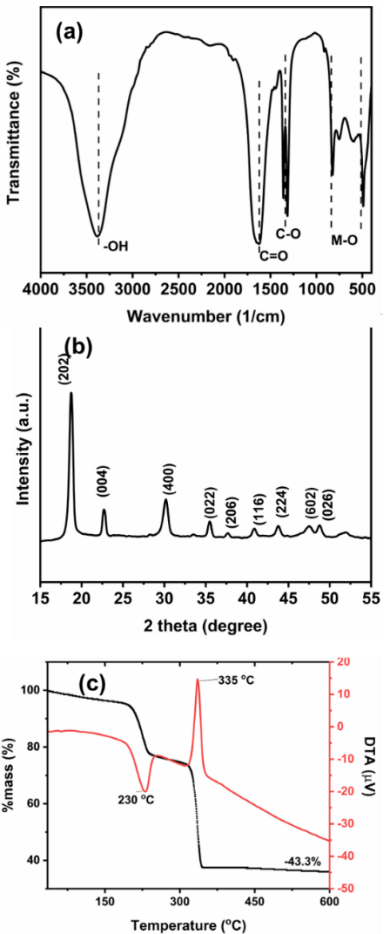
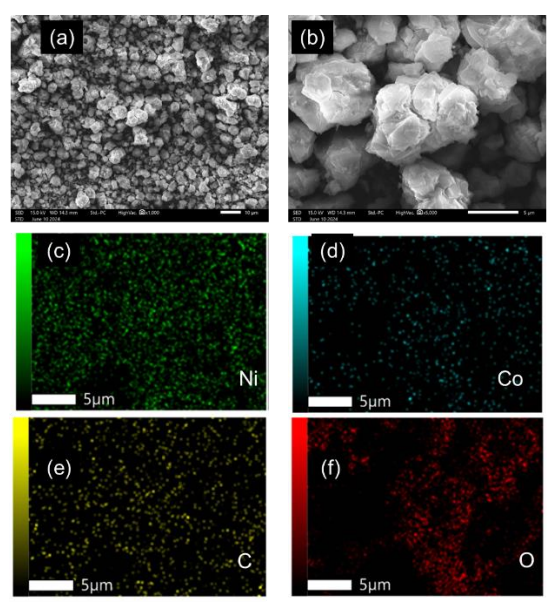


Fig. 3 (a) FTIR Spectra, (b) XRD pattern, and (c) TG/DTA curve of NC precursor

the successful formation of metal-oxalate coordination complexes, evidenced by the characteristic vibrational modes at specific wavenumbers (Nisa *et al.*, 2022). The strong absorption band at 3400 cm<sup>-1</sup> corresponds to the hydration water molecules, while the well-defined peaks at 1620 cm<sup>-1</sup> and 1320 cm<sup>-1</sup> represent the C=O and C-O stretching vibrations, respectively. The presence of M-O vibrations in the lower wavenumber region (500-800 cm<sup>-1</sup>) confirms the successful coordination between the metal cations and oxalate ligands, demonstrating the effectiveness of the simple oxalate precipitation route (Zeng & Zhang, 2020).

The X-ray diffraction analysis examines the precursor's phase purity and crystallinity, which exhibits well-defined diffraction peaks of nickel oxalate dihydrate or JCPDS card no. 00-025-0582 (Oh  $et\ al.$ , 2016). The prominent (202) reflection at  $2\theta\approx18.5^\circ$  and subsequent crystallographic planes demonstrate the formation of a single-phase material without any detectable impurities, even with the significant amount of Co in the sample. The sharp diffraction peaks indicate the high crystallinity achieved through the controlled precipitation process, highlighting the efficiency of our synthetic approach in producing high-quality precursor materials (Zhu  $et\ al.$ , 2020).

Thermal analysis provides crucial insights into the precursor's decomposition behavior and stability. The TG/DTA profiles reveal a well-defined two-step decomposition process with distinct thermal events at 230°C and 335°C. The initial endothermic peak corresponds to the gradual removal of crystalline water, while the sharp exothermic peak at 335°C



**Fig. 4** Morphological and elemental analysis of NC precursor: (a,b) SEM images at different magnifications, and (c-f) corresponding EDX elemental mapping showing the distribution of Ni, Co, C, and O elements.

corresponds to the rapid decomposition of the anhydrous oxalate species.

$$Ni_{0.8}Co_{0.2}C_2O_4 \cdot 2H_2O \rightarrow Ni_{0.8}Co_{0.2}C_2O_4 + 2H_2O \uparrow$$
 (5)

$$Ni_{0.8}Co_{0.2}C_2O_4 \rightarrow Ni_{0.8}Co_{0.2}O + CO\uparrow + CO_2\uparrow$$
 (6)

The precise weight loss of 43.3% is well aligned with theoretical calculations, confirming the stoichiometric composition and phase purity of the precursor. This controlled thermal behavior is particularly advantageous for subsequent processing steps in cathode material synthesis(Zhu *et al.*, 2020).

Figure 4 displays the morphological characteristics of NC precursor. The SEM images demonstrate the formation of uniform, well-defined polyhedral particles with sizes ranging from 2-5 µm. The crystallites exhibit smooth surfaces and distinct facets, indicating controlled crystal growth during the precipitation process. The observed morphology suggests optimal nucleation and growth kinetics achieved through our simplified synthesis approach. Higher magnification images further reveal the intricate layered structure of individual particles, which is beneficial for subsequent thermal conversion to the oxide phase.

The elemental distribution, mapped through EDX analysis, confirms the remarkable homogeneity of the binary metal system. The uniform distribution of Ni and Co, maintaining the designed 4:1 ratio, indicates the effectiveness of

the co-precipitation strategy in achieving atomic-level mixing. The consistent carbon and oxygen distribution correlates well with the oxalate chemical structure. The absence of elemental segregation or clustering demonstrates the excellent chemical homogeneity achieved through this straightforward synthetic route (Zeng & Zhang, 2020).

These comprehensive characterization results show the successful synthesis of high-quality Ni<sub>0.8</sub>Co<sub>0.2</sub>C<sub>2</sub>O<sub>4</sub>·2H<sub>2</sub>O precursor through a simplified oxalate precipitation method. The achieved phase purity, crystallinity, and compositional homogeneity are excellent, considering the simplicity of the synthesis process. These characteristics make the precursor ideally suited for high-performance cathode materials, while the simple synthetic approach offers significant advantages for potential scale-up and industrial implementation (Nisa *et al.*, 2022).

#### 3.3 Analysis of NCAF Cathode Material

#### 3.3.1 Analysis of Crystal Structure Test (XRD)

X-ray diffraction analysis systematically investigated the synthesized materials' phase structure and crystallinity. Figure 5a shows the XRD result of NCAF samples. All samples exhibit well-defined diffraction patterns characteristic of the  $\alpha$ -NaFeO2 structure (R-3m space group), which is also identical to NCA (JCPDS 87-1562). Based on the lattice parameter analysis in Table 3, all of the NCAF samples exhibit hexagonal and layered oxide material. The sharp diffraction peaks across all samples can be attributed to the high crystalline properties of the samples. In Figure 5(b and c), The clear splitting of the (006)/(012) and (018)/(110) peaks indicates the preservation of the well-ordered layered structure up to 5% AFH incorporation. The refined structural parameters in Table 3 show structural changes with increasing AFH content. The intensity ratio (I(003)/I(104)) decreases from 1.91 to 1.62, indicating increased but still acceptable cation mixing, as values remain well above the critical threshold of 1.2. The c/a ratio shows a gradual increase from 4.93 to 4.99, reflecting the successful incorporation of Fe3+ ions into the layered structure (Yudha, Hutama, et al., 2022). Crystallite size initially decreases from 73.8 nm to 55.72 nm at 5% AFH, suggesting that moderate doping promotes finer crystallite formation. The systematic increase in unit cell volume (381.98 to 393.26 ų) confirms the effective incorporation of larger Fe3+ ions while maintaining structural integrity (H. Zhang et al., 2022). These structural modifications demonstrate successful AFH doping while preserving the fundamental layered oxide structure crucial for electrochemical performance (Wang et al., 2023).

A notable structural evolution is observed with increasing AFH content, particularly in NCAF7.5, where the emergence of a weak reflection at 43-44° indicates the formation of a minor LiFeO2 phase(Abdel-Ghany *et al.*, 2012). This suggests that

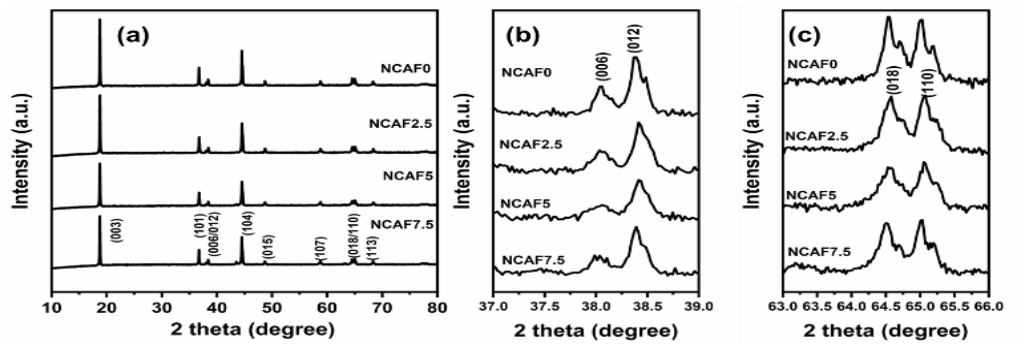


Fig. 5 XRD patterns of NCAF samples: (a) full and enlarged views of (b) (006)/(012) and (c) (018)/(110) peak regions

**Table 3**NCAF Samples Structural and Lattice Parameters

NCAL Samples Structural and Lattice Farameters						
Sample	I ratio	c/a	Crystallite	Cell		
			size	volume		
			(nm)	(ų)		
NCAF0	1.91	4.93	73.8	381.98		
NCAF2.5	1.88	4.96	63.74	387.68.		
NCAF5	1.72	4.98	55.72	390.21		
NCAF7.5	1.62	4.99	62.32	393.26		

while the layered structure can accommodate AFH doping up to 5%, higher concentrations lead to phase impurity, establishing an optimal doping range for maintaining structural integrity (Ma et~al., 2012). The systematic evolution of peak positions and intensities with increasing AFH content, coupled with the occurrence of the secondary phase at higher doping levels, provides valuable insights into the structural limits of AFH incorporation. This finding is particularly significant for optimizing the waste utilization strategy, indicating that moderate AFH doping ( $\leq$ 5%) can be effectively achieved without compromising the primary layered structure.

#### 3.3.2 FTIR analysis

The FTIR spectra of the synthesized NCAF samples displayed in Figure 6 show characteristic vibrational features of the layered oxide structure. All compositions exhibit bands in the low-frequency region (500-700 cm<sup>-1</sup>) corresponding to metal-oxygen (M-O) stretching vibrations, indicating the formation of the desired oxide framework. A notable observation across all samples is the presence of carbonate (CO3<sup>2-</sup>) absorption bands around 1450-1500 cm<sup>-1</sup>, suggesting minor surface carbonate formation due to atmospheric exposure, which is commonly observed in Ni-rich layered oxides. The intensity of these carbonate bands remains relatively constant across NCAF0 through NCAF5, but shows a slight increase in NCAF7.5, potentially indicating enhanced surface reactivity at higher AFH content. The absence of significant hydroxyl (-OH) stretching bands in the 3000-3500

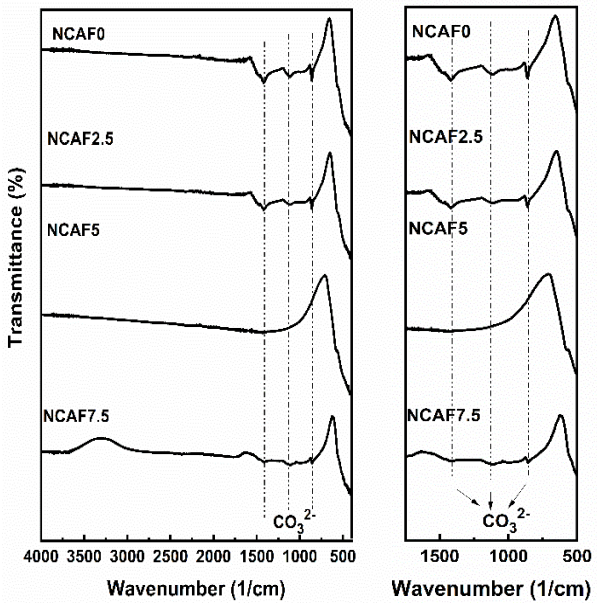


**Fig. 6** FTIR Spectra Results of NCAF0, NCAF2.5, NCAF5, and NCAF7.5 Materials

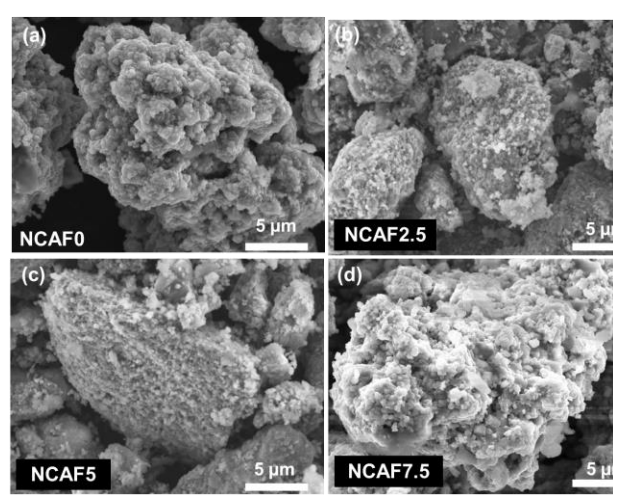


Fig. 7 SEM Images of NCAF samples

cm<sup>-1</sup> region confirms the complete conversion of the precursors to oxide phases during high-temperature synthesis (Yudha, Hutama, *et al.*, 2022).

# 3.3.3 Morphological Characterization and Element Analysis of NCAF

The surface morphology and particle characteristics of the NCAF samples were investigated using scanning electron microscopy and presented in Figure 7, showing distinct changes with increasing AFH content. The pristine NCAF0 sample exhibits well-defined secondary particles with a characteristic hierarchical structure composed of densely packed primary particles, displaying a relatively uniform surface texture. Upon incorporation of AFH, notable morphological modifications are observed. NCAF2.5 maintains similar secondary particle shape with smaller size (approximately 12 µm) but shows slightly increased surface roughness compared to the pristine sample. At 5% AFH incorporation (NCAF5), the particles demonstrate enhanced surface porosity while maintaining the overall secondary particle architecture, suggesting successful integration of dopants without significant structural disruption. However, NCAF7.5 shows clearer morphological changes with increased agglomeration and irregular surface features, consistent with the formation of the secondary phase observed in XRD analysis. This evolution of particle morphology indicates that while moderate AFH doping (≤5%) can be accommodated within the structure without significant morphological deterioration, higher doping levels lead to notable changes in particle characteristics.

Figure 8 and Table 4 display the surface area analysis result. The nitrogen adsorption-desorption isotherms and corresponding surface analysis reveal significant changes in the surface characteristics with increasing AFH content. The pristine NCAF0 exhibits a type IV isotherm with an H3 hysteresis loop, characteristic of mesoporous materials, showing the highest specific surface area (BET: 38.747 m<sup>2</sup>/g, BJH: 61.466 m<sup>2</sup>/g) among all samples. These values are substantially higher than commercial NCA materials (typically <5 m<sup>2</sup>/g), indicating a more exposed surface structure that could lead to increased reactivity with the electrolyte (Thapa et al., 2022). The decomposition of oxalates (NC precursor) during the sintering can cause severe pore formation, resulting in a high surface area. Upon initial AFH incorporation, NCAF2.5 maintains a similar isotherm shape but shows a slight decrease in surface area (BET: 36.92 m²/g, BJH: 34.9 m²/g). However, a

**Table 4**Surface Area Analysis of NCAF samples

buriace Area Analysis of NeAr samples						
	Surface		Average			
	BET	Surface BJH	Pore			
Samples	$(m^2/g)$	$(m^2/g)$	(nm)			
NCAF0	38.747	61.466	8.73			
NCAF2.5	36.92	34.9	8.64			
NOAFE	6.50	4.05	0.70			
NCAF5	6.52	4.25	9.73			
NCAF7.5	9.52	1.67	13.62			

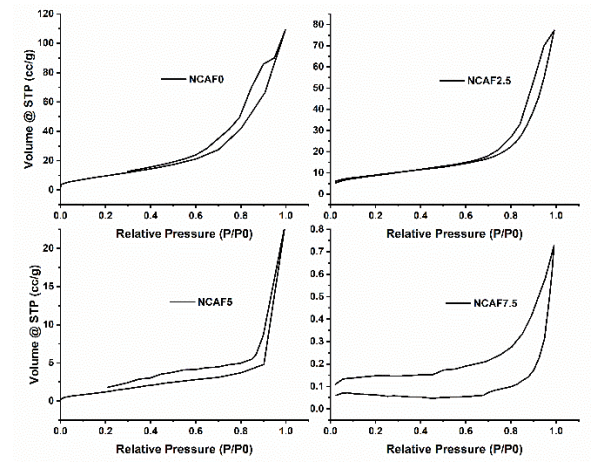


**Fig. 8** N2 adsorption-desorption isotherms of NCAF samples with different AFH content (0%, 2.5%, 5%, and 7.5%)

dramatic change is observed with higher AFH content, where NCAF5 and NCAF7.5 show significantly reduced surface areas (6.52 and 9.52  $\rm m^2/g$  BET, respectively) and increasing average pore sizes (9.73 and 13.62 nm, respectively) (Hu *et al.*, 2020). These phenomena indicate that the addition of AFH could increase the binding effect, resulting in an agglomeration of the sample.

Surface characteristics, especially the surface area, significantly affect electrochemical performance. NCAF0 and NCAF2.5 show much higher surface areas than commercial materials, which could potentially lead to accelerated surface side reactions and capacity fading, the significant reduction in surface area with higher AFH content (NCAF5 and NCAF7.5) brings these materials closer to commercial specifications (C. Liu et al., 2018). This suggests that higher AFH doping may be beneficial from a surface stability perspective, despite the formation of secondary phases observed in XRD. The larger pore sizes in heavily doped samples, coupled with reduced surface area, might provide a better balance between electrolyte accessibility and surface stability, more closely resembling the characteristics that make commercial NCA materials successful in long-term applications (C. Liu et al., 2018). EDX analysis result in Table 5 confirms the successful incorporation of AFH as Al and Fe dopants into the layered oxide structure of NCA. It is used to identify the final composition of NCAF cathode material presented in Table 6. The pristine NCAF0 exhibits the designed composition of LiNi<sub>0.8</sub>Co<sub>0.2</sub>O<sub>2</sub>, with Ni:Co ratio closely matching the target values (0.80:0.20). Upon AFH incorporation, systematic compositional evolution is observed, yielding  $LiNi_{0.75}Co_{0.18}Al_{0.03}Fe_{0.04}O_{2}$ ,  $LiNi_{0.70}Co_{0.17}Al_{0.05}Fe_{0.08}O_{2}$ ,  $LiNi_{0.66}Co_{0.16}Al_{0.08}Fe_{0.10}O_{2}\ for\ NCAF2.5,\ NCAF5,\ and\ NCAF7.5,$ respectively. The progressive decrease in Ni and Co content corresponds well with the increasing Al and Fe substitution.

# 3.3.4 Electrochemical Performance Analysis of NCAF in fullcylindrical cell

dQ/dV analysis of NCAF sample in full Li-ion battery cells is investigated to understand the effect of AFH composition towards the electrochemical behavior of the cell. Figure 9 presents a dQ/dV plot which characterizes the reduction and oxidation (redox) behavior of the NCAF/graphite full cells during the formation step or in the first cycle, using a DC current density of 10 mA/g. The pristine NCAF0 shows typical NCA-

**Table 5** Atomic Composition of NCAF Materials

A +		NCAF0		NCAF2.5		NCAF2.5		NCAF7.5	
Atom	mol	mass	mol	mass	mol	mass	mol	mass	
Ni	0.357	0.605	0.331	0.562	0.308	0.523	0.287	0.487	
Со	0.101	0.171	0.093	0.159	0.087	0.148	0.081	0.138	
Al	0.000	0.000	0.026	0.020	0.049	0.038	0.071	0.055	
Fe	0.000	0.000	0.019	0.031	0.036	0.058	0.052	0.084	
O	0.542	0.224	0.531	0.228	0.520	0.233	0.509	0.236	
Total	1.000	1.000	1.000	1.000	1.000	1.000	1.000	1.000	

**Table 6**Estimated Product composition

	1				
Sample	Ni	Со	Al	Fe	Compound
NCAF0	0.799	0.201	0	0	$LiNi_{0.8}Co_{0.2}O_2 \\$
NCAF2.5	0.747	0.187	0.0275	0.038	$LiNi_{0.75}Co_{0.18}Al_{0.03}Fe_{0.04}O_{2} \\$
NCAF5	0.699	0.176	0.0526	0.073	$LiNi_{0.70}Co_{0.17}Al_{0.05}Fe_{0.08}O_{2} \\$
NCAF7.5	0.656	0.165	0.0754	0.105	LiNin 66Con 16Aln 08Fen 10O2

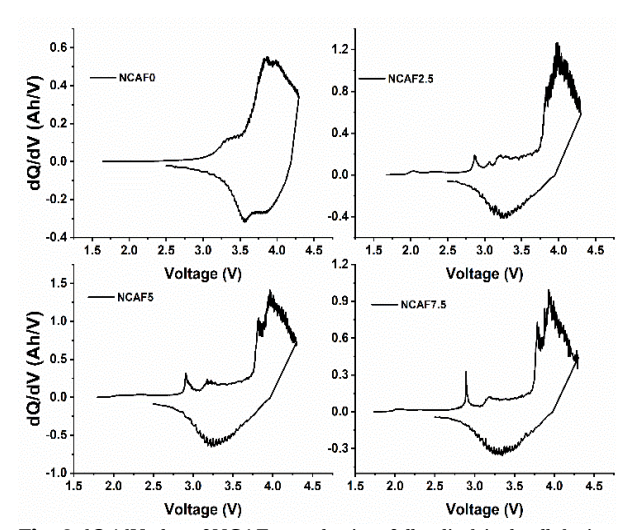
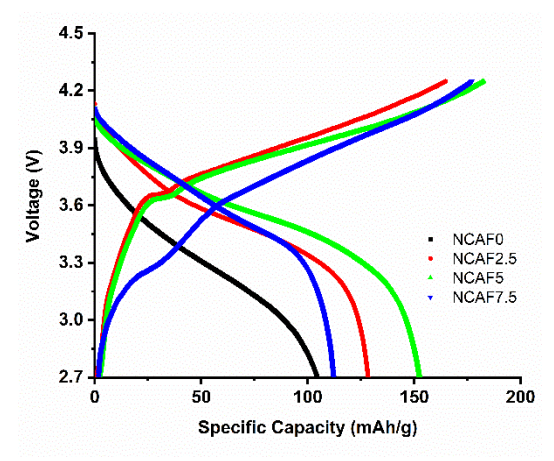


Fig. 9 dQ/dV plot of NCAF samples in a full cylindrical cell during the formation step

graphite electrochemical features with a primary oxidation peak at ~4.0V and reduction peak at ~3.7V, corresponding to the Ni<sup>2+</sup>/Ni<sup>3+</sup>/Ni<sup>4+</sup> redox couples overlapped with graphite deintercalation/intercalation processes (Pathan et al., 2019). Upon AFH incorporation, observable changes in the redox profiles are observed. NCAF2.5 maintains similar peak positions but shows slightly broadened peaks, indicating modified reaction kinetics with initial doping (Hashem et al., 2019). NCAF5 and NCAF7.5 exhibit additional redox features around 2.5-3.0V and clear cathodic peak splitting at 3.7-3.9 V, likely associated with electrolyte decomposition and Fe3+/Fe4+ redox activity at higher AFH content. The peak intensity gradually decreases with increasing AFH content from 5% to 7.5%; with higher AFH content, the Ni content is reduced, affecting the overall capacity. Notably, the well-maintained peak separation across all compositions suggests moderate AFH doping preserves the fundamental redox mechanisms while successfully incorporating additional electrochemically active Fe species (Park et al., 2020).

The initial charge-discharge profiles in Figure 10 show distinct electrochemical behaviors across the NCAF series in full-cell configuration. NCAF0 shows a typical voltage profile of Ni-rich cathodes paired with graphite, delivering a specific capacity of ~110 mAh/g with a smooth voltage slope. Interestingly, the AFH-doped samples demonstrate enhanced



 $\textbf{Fig. 10} \ \ \text{Charge and Discharge Curve of NCAF samples in a full cylindrical cell during the formation step}$ 

capacity, with NCAF2.5, NCAF5, and NCAF7.5 achieving ~127, ~155, and ~111 mAh/g, respectively. This trend correlates well with the dQ/dV analysis, where the emergence of additional redox features around 3.0V in doped samples, particularly visible in NCAF5 and NCAF7.5, contributes to the increased capacity through iron doping(Nurohmah *et al.*, 2021).

The voltage profiles also show characteristic plateaus corresponding to the significant redox peaks observed in dQ/dV plots. The main plateau around 3.7-4.0V represents the Ni²+/Ni³+/Ni⁴+ reactions, which becomes less clear with increasing AFH content, consistent with the decreasing Ni content confirmed by EDX. NCAF5 exhibits the most balanced profile with optimal capacity, suggesting that moderate AFH doping enhances electrochemical performance through synergistic effects of Al stabilization and Fe redox contribution. In contrast, excessive doping in NCAF7.5 leads to capacity decrease, likely due to the formation of the LiFeO2 phase observed in XRD. Based on this data, the estimated reaction during the initial charge and discharge can be expressed in the equations below.

Charging step:

$$\begin{array}{l} \text{LiNi}_{0.8\text{-x-y}}\text{Co}_{0.2\text{-z}}\text{Al}_y\text{Fe}_z\text{O}_2 \to \\ \text{Li}_{1\text{-}}\delta\text{Ni}_{0.8\text{-x-y}}\text{Co}_{0.2\text{-z}}\text{Al}_y\text{Fe}_z\text{O}2 + \delta\text{Li}^+ + \delta\text{e}^- \end{array} \tag{7}$$

$$6C + xLi^{+} + xe^{-} \rightarrow Li_{x}C_{6}$$
 (8)

Discharging step:

$$Li_xC_6 \rightarrow 6C + xLi^+ + xe^- \tag{9}$$

$$\begin{array}{l} \text{Li}_{1\text{-}\delta}\text{Ni}_{0.8\text{-x-y}}\text{Co}_{0.2\text{-z}}\text{Al}_y\text{Fe}_z\text{O2} + \delta\text{Li}^+ + \delta\text{e}^- \rightarrow \\ \text{Li}\text{Ni}_{0.8\text{-x-y}}\text{Co}_{0.2\text{-z}}\text{Al}_y\text{Fe}_z\text{O2} \end{array} \tag{10}$$

Whereas  $\delta$  is the actual reversible Li which represents the actual capacity of NCAF.

#### 4. Conclusion

This study demonstrates a novel approach for high-nickel cathode material development through the successful incorporation of coal fly ash waste-derived Al/Fe hydroxides (AFH) during the synthesis of lithium nickel cobalt aluminum iron oxide (NCAF). The characterization of samples prepared at various AFH compositions confirms:

- The formation of high-purity materials within the  $\alpha$ -NaFeO2 structure (R-3m space group) up to 5% AFH content, while higher doping leads to LiFeO2 phase formation. The decrease in  $I_{(003)}/I_{(104)}$  ratio (1.91 to 1.62) and increase in cell volume (381.98 to 393.26 ų) verify effective dopant incorporation while maintaining structural integrity.
- The surface area decreased from 38.747 m²/g to 6.52 m²/g with increasing AFH content which approaches commercial-grade specifications, suggesting optimized particle characteristics.
- The compositional transition from LiNi $_{0.8}$ Co $_{0.2}$ O $_2$  to LiNi $_{0.66}$ Co $_{0.16}$ Al $_{0.08}$ Fe $_{0.10}$ O $_2$  maintains uniform elemental distribution,
- The optimal specific capacity for NCAF is at 5% AFH composition (~155 mAh/g), attributed to synergistic Al stabilization and Fe redox contribution.

These findings establish a viable pathway for valorizing industrial waste in high-performance battery materials, effectively combining technological advancement with environmental concerns. Material enhancement through process parameter optimization, i.e. Sintering temperature and

time and mixing time, is crucial for future investigation. In addition, Life cycle analysis (LCA) of fly ash utilization for NCAF is also important to assure the sustainability level before industrial scale implementation.

**Author Contributions**: CSY; Conceptualization, supervision, resources, project administration, writing—review and editing, project administration, validation. ADR, RS and MA.: Data curation, methodology, formal analysis, writing—original draft. SUM and APL: Formal analysis, validation, writing—review and editing. All authors have read and agreed to the published version of the manuscript.

**Funding:** This research was funded by Lembaga Penelitian dan Pengembangan Masyarakat (LPPM) of Universitas Sebelas Maret through Mitrasmart Collaboration Research (Riset Kolaborasi Mitrasmart) with contract number: 194.2/UN27.22/PT.01.03/2024. The authors also acknowledge the support of Enni Apriliyani.

**Conflicts of Interest:** The authors declare no conflict of interest.

#### References

- Abdel-Ghany, A. E., Mauger, A., Groult, H., Zaghib, K., & Julien, C. M. (2012). Structural properties and electrochemistry of α-LiFeO2. *Journal of Power Sources*, 197, 285–291. https://doi.org/10.1016/j.jpowsour.2011.09.054
- Chandrasekharam, D., Şener, M. F., Recepoğlu, Y. K., Isık, T., Demir, M. M., & Baba, A. (2024). Lithium: An energy transition element, its role in the future energy demand and carbon emissions mitigation strategy. *Geothermics*, 119. https://doi.org/10.1016/j.geothermics.2024.102959
- Hashem, A. M., Abdel-Ghany, A. E., Scheuermann, M., Indris, S., Ehrenberg, H., Mauger, A., & Julien, C. M. (2019). Doped nanoscale NMC333 as cathode materials for Li-ion batteries. *Materials*, 12(18). https://doi.org/10.3390/ma12182899
- He, K., Ruan, Z., Teng, X., & Zhu, Y. (2017). Facile synthesis and electrochemical properties of spherical LiNi0.85-xCo0.15AlxO2 with sodium aluminate via co-precipitation. *Materials Research Bulletin*, 90, 131–137. https://doi.org/10.1016/j.materresbull.2017.01.039
- He, X., Qiu, X., & Chen, J. (2017). Preparation of Fe(II)–Al layered double hydroxides: Application to the adsorption/reduction of chromium. Colloids and Surfaces A: Physicochemical and Engineering Aspects, 516, 362–374. https://doi.org/10.1016/j.colsurfa.2016.12.053
- Hu, J. P., Sheng, H., Deng, Q., Ma, Q., Liu, J., Wu, X. W., Liu, J. J., & Wu, Y. P. (2020). High-rate layered cathode of lithium-ion batteries through regulating three-dimensional agglomerated structure. *Energies*, 13(7). https://doi.org/10.3390/en13071602
- Hwang, I., Lee, C. W., Kim, J. C., & Yoon, S. (2012). Particle size effect of Ni-rich cathode materials on lithium ion battery performance. *Materials Research Bulletin*, 47(1), 73–78. https://doi.org/10.1016/j.materresbull.2011.10.002
- Jumari, A., Yudha, C. S., Widiyandari, H., & Lestari, A. P. (2020). SiO2/C Composite as a High Capacity Anode Material of LiNi0.8Co0.15Al0.05O2 Battery Derived from Coal Combustion Fly Ash. Applied Science, 10(23), 1–13. https://doi.org/10.3390/app10238428
- Kim, C., Park, T.-J., Min, S.-G., Yang, S.-B., & Son, J.-T. (2014). Effects of iron doping at 55 °C on LiNio.85Coo.10Alo.05O2. *Journal of the Korean Physical Society*, 65(2), 243–247. https://doi.org/10.3938/jkps.65.243
- Lagouir, M., Badri, A., & Sayouti, Y. (2021). Multi-objective optimization dispatch based energy management of a microgrid running under grid connected and standalone operation mode.

- International Journal of Renewable Energy Development, 10(2), 333–343. https://doi.org/10.14710/ijred.2021.34656
- Liu, C., Qian, K., Lei, D., Li, B., Kang, F., & He, Y.-B. (2018). Deterioration mechanism of LiNi0.8Co0.15Al0.05O2/graphite–SiOx power batteries under high temperature and discharge cycling conditions. *Journal of Materials Chemistry A*, 6(1), 65–72. https://doi.org/10.1039/C7TA08703A
- Liu, X., Zhang, Q., Zhu, Y., Zhao, J., Chen, J., Ye, H., Wei, H., & Liu, Z. (2022). Trash to Treasure: Harmful Fly Ash Derived Silicon Nanoparticles for Enhanced Lithium-Ion Batteries. Silicon, 14(13), 7983–7990. https://doi.org/10.1007/s12633-021-01528-
- Lv, Y., Cheng, X., Qiang, W., & Huang, B. (2020). Improved Electrochemical Performances of Ni-rich LiNi0.83Co0.12Mn0.05O2 by Mg-doping. Journal of Power Sources, 450(January), 227718. https://doi.org/10.1016/j.jpowsour.2020.227718
- Ma, Y., Zhu, Y., Yu, Y., Mei, T., Xing, Z., Zhang, X., & Qian, Y. (2012). Low temperature synthesis of α-LiFeo 2 nanoparticles and its behavior as cathode materials for Li-ion batteries. *International Journal of Electrochemical Science*, 7(5), 4657–4662. https://doi.org/10.1016/s1452-3981(23)19570-8
- Mathapati, M., Amate, K., Durga Prasad, C., Jayavardhana, M. L., & Hemanth Raju, T. (2021). A review on fly ash utilization. *Materials Today: Proceedings, xxxx*. https://doi.org/10.1016/j.matpr.2021.09.106
- Mopoung, S., Sitthikhankaew, R., & Mingmoon, N. (2021). Preparation of anode material for lithium battery from activated carbon. International Journal of Renewable Energy Development, 10(1), 91–96. https://doi.org/10.14710/ijred.2021.32997
- Mu, G., Agrawal, S., Sittisomwong, P., & Bai, P. (2022). Impacts of negative to positive capacities ratios on the performance of nextgeneration lithium-ion batteries. *Electrochimica Acta*, 406. https://doi.org/10.1016/j.electacta.2022.139878
- Muzayanha, S. U., Yudha, C. S., Nur, A., Widiyandari, H., Haerudin, H., Nilasary, H., Fathoni, F., & Purwanto, A. (2019). A fast metals recovery method for the synthesis of lithium nickel cobalt aluminum oxide material from cathode waste. *Metals*, 9(5). https://doi.org/10.3390/met9050615
- Nisa, S. S., Nurohmah, A. R., Yudha, C. S., Nilasary, H., Nursukatmo, H., Dyartanti, E. R., & Purwanto, A. (2021). Utilization of Spent Nickel Catalyst as Raw Material for Ni-Rich Cathode Material. *Jurnal Presipitasi: Media Komunikasi Dan Pengembangan Teknik Lingkungan,* 18(2), 349–357. https://doi.org/10.14710/presipitasi.v18i2.349-357
- Nisa, S. S., Rahmawati, M., Yudha, C. S., Nilasary, H., Nursukatmo, H., Oktaviano, H. S., Muzayanha, S. U., & Purwanto, A. (2022). Fast Approach to Obtain Layered Transition-Metal Cathode Material for Rechargeable Batteries. *Batteries*, 8(1). https://doi.org/10.3390/batteries8010004
- Nurohmah, A. R., Yudha, C. S., Rahmawati, M., Nisa, S. F. S., Jumari, A., Widiyandari, H., & Purwanto, A. (2021). Structural and electrochemical analysis of iron doping in lini0.6-xmn0.2co0.2fexo2 battery. *Evergreen*, 8(1), 82–88. https://doi.org/10.5109/4372263
- Oh, H. J., Jo, C. H., Yoon, C. S., Yashiro, H., Kim, S. J., Passerini, S., Sun, Y. K., & Myung, S. T. (2016). Nickel oxalate dihydrate nanorods attached to reduced graphene oxide sheets as a high-capacity anode for rechargeable lithium batteries. NPG Asia Materials, 8(5). https://doi.org/10.1038/am.2016.59
- Park, S., Jo, C., Kim, H. J., Kim, S., Myung, S. T., Kang, H. K., Kim, H., Song, J., Yu, J., & Kwon, K. (2020). Understanding the role of trace amount of Fe incorporated in Ni-rich Li[Ni1-x-yCoxMny]O2 cathode material. *Journal of Alloys and Compounds*, 835. https://doi.org/10.1016/j.jallcom.2020.155342
- Pathan, T. S., Rashid, M., Walker, M., Widanage, W. D., & Kendrick, E. (2019). Active formation of Li-ion batteries and its effect on cycle life. JPhys Energy, 1(4). https://doi.org/10.1088/2515-7655/ab2e92
- Purwanto, A., Yudha, C. S., Ubaidillah, U., Widiyandari, H., & Ogi, T. (2018). NCA cathode material: synthesis methods and performance enhancement efforts NCA cathode material: synthesis methods and performance enhancement efforts.

- Materials Research Express, 5(12), 122001. https://doi.org/10.1088/2053-1591/aae167
- Rahmawati, F., Alaih, I. S., Rosalin, A. W., Nurcahyo, I. F., Nursukatmo, H., Nilasary, H., Oktaviano, H. S., Raihan, E., Muzayanha, S. U., & Handaka, M. F. A. (2024). A dry cold sintering to Ta doped-lithium lanthanum zirconate solid electrolyte for all-solid-state lithium metal battery. *International Journal of Renewable Energy Development*, 13(5), 959. https://doi.org/10.61435/ijred.2024.60351
- Seenivasan, M., Jeyakumar, J., Wu, Y. S., Pham, Q. T., Chern, C. S., Hwang, B. J., & Yang, C. C. (2022). Bifunctional coating layer on Ni-rich cathode materials to enhance electrochemical performance and thermal stability in lithium-ion batteries. Composites Part B: Engineering, 242. https://doi.org/10.1016/j.compositesb.2022.110083
- Sudaryanto, Salsabila, N., Sari, P. A. K., Fachrudin, A. C., Salsabila, A. A., Nursanto, E. B., Priyono, S., Jodi, H., & Gumelar, M. D. (2024). Comparison of lithium sources on the electrochemical performance of LiNi0.5Mn1.5O4 cathode materials for lithiumion batteries. *International Journal of Renewable Energy Development*, 13(3), 448–456. https://doi.org/10.61435/ijred.2024.59662
- Thapa, A. K., Lavery, B. W., Hona, R. K., Sapkota, N., Kalutara Koralalage, M., Adeniran, A., Ajayi, B. P., Zain, M. A., Wang, H., Druffel, T., Jasinski, J. B., Sumanasekera, G. U., Sunkara, M. K., & Yoshio, M. (2022). Mn-Rich NMC Cathode for Lithium-Ion Batteries at High-Voltage Operation. *Energies*, 15(22). https://doi.org/10.3390/en15228357
- Wan, D. Y., Fan, Z. Y., Dong, Y. X., Baasanjav, E., Jun, H., Jin, B., Jin, E. M., & Jeong, S. M. (2018). Effect of Metal (Mn, Ti) Doping on NCA Cathode Materials for Lithium Ion Batteries. *Journal of Nano Materials*, 2018, 082502, https://doi.org/10.1155/2018/8082502
- Wang, J., Zhou, G., Hou, S., Wei, S., Li, Y., Dong, S., Yan, X., Zhao, D., & Hou, X. (2023). A novel method to preparing LiNi0.8Co0.15Al0.05O2 cathode materials using nano-sized Al(OH)3. *Materials Letters*, 335. https://doi.org/10.1016/j.matlet.2023.133816
- Xie, H., Du, K., Hu, G., Duan, J., Peng, Z., Zhang, Z., & Cao, Y. (2015). Synthesis of LiNi0.8Co0.15Al0.05O2with 5-sulfosalicylic acid as

- a chelating agent and its electrochemical properties. *Journal of Materials Chemistry A*, *3*(40), 20236–20243. https://doi.org/10.1039/c5ta05266a
- Xie, H., Hu, G., Du\*, K., Peng, Z., & Cao, Y. (2016). An improved continuous co-precipitation method to synthesize LiNi0.8Al0.05O2 cathode material. *Journal of Alloys and Compounds*, 666, 84–87. https://doi.org/10.1016/j.jallcom.2016.01.064
- Yudha, C. S., Apriliyani, E., Paramitha, T., Suci, W. G., & Gustiana, H. S. E. A. (2022). Recovery of Valuable Metals from Fly Ash via Hydrometallurgy Method for Li-ion Battery Anode Material. JKPK (Jurnal Kimia Dan Pendidikan Kimia), 7(3), 265. https://doi.org/10.20961/jkpk.v7i3.64740
- Yudha, C. S., Hutama, A. P., Rahmawati, M., & Arinawati, M. (2022).
  Production of nickel-rich LiNi0.89Co0.08Al0.03O2 cathode material for high capacity NCA / graphite secondary battery fabrication.
  Open Engineering, 12, 501–510.
  https://doi.org/10.1515/eng-2022-0051
- Zeng, T., & Zhang, C. (2020). An effective way of co-precipitating Ni2+, Mn2+ and Co2+ by using ammonium oxalate as precipitant for Ni-rich Li-ion batteries cathode. *Journal of Materials Science*, 55(25), 11535–11544. https://doi.org/10.1007/s10853-020-04753-w
- Zhang, H., Wang, X., Naveed, A., Zeng, T., Zhang, X., Shi, H., Su, M., Dou, A., Zhou, Y., & Liu, Y. (2022). Comparison of structural and electrochemical properties of LiNio.8Coo.15Alo.05O2 with Li site doping by different cations. *Applied Surface Science*, 599. https://doi.org/10.1016/j.apsusc.2022.153933
- Zhang, Y., Li, M., Liu, D., Hou, X., Zou, J., Ma, X., Shang, F., & Wang, Z. (2019). Aluminum and iron leaching from power plant coal fly ash for preparation of polymeric aluminum ferric chloride. Environmental Technology (United Kingdom), 40(12), 1568–1575. https://doi.org/10.1080/09593330.2018.1426639
- Zhu, J., Cao, G., Li, Y., Xi, X., Jin, Z., Xu, B., & Li, W. (2020). Efficient utilisation of rod-like nickel oxalate in lithium-ion batteries: A case of NiO for the anode and LiNiO2 for the cathode. *Scripta Materialia*, 178(3), 51–56. https://doi.org/10.1016/j.scriptamat.2019.10.051



© 2025. The Author(s). This article is an open access article distributed under the terms and conditions of the Creative Commons Attribution-ShareAlike 4.0 (CC BY-SA) International License (http://creativecommons.org/licenses/by-sa/4.0/)